http://dx.doi.org/10.6113/TKPE.2015.20.1.91

계통 불평형시 과도 응답 특성이 개선된 고압 이중여자 유도형 풍력발전 시스템의 제어 전략

한대수[1], 서용석†

Control Strategy of Improved Transient Response for a Doubly Fed Induction Generator in Medium Voltage Wind Power System under Grid Unbalance

Dae-Su Han[1] and Yong-Sug Suh†

Abstract

This paper investigates control algorithms for a doubly fed induction generator with a back-to-back three-level neutral-point clamped voltage source converter in a medium-voltage wind power system under unbalanced grid conditions. Negative sequence control algorithms to compensate for unbalanced conditions have been investigated with respect to four performance factors: fault ride-through capability, instantaneous active power pulsation, harmonic distortions, and torque pulsation. The control algorithm having zero amplitude of torque ripple indicates the most cost-effective performance in terms of torque pulsation. The least active power pulsation is produced by a control algorithm that nullifies the oscillating component of the instantaneous stator active and reactive power. A combination of these two control algorithms depending on operating requirements and depth of grid unbalance presents the most optimized performance factors under generalized unbalanced operating conditions, leading to a high-performance DFIG wind turbine system with unbalanced grid adaptive features.

Key words: Converter, DFIG, Unbalanced grid conditions, Wind power system

1. Introduction

Wind power system is one of the fastest growing renewable energy systems. Wind power installation has been increasing both in number and size of individual wind turbine. Among various types of wind turbine system, Doubly Fed Induction Generator (DFIG) is widely used as wind generator due to its economic requirement of power converter in rotor side. Typically a power converter having 25% ~ 30% of the generator rating is employed in rotor side of DFIG to meet the variable speed range of wind turbine. Because of the direct connection between the stator and grid, the unbalanced grid voltage causes unbalanced stator currents. The unbalanced currents generate unequal heating of the stator windings and oscillations of torque resulting in a mechanical stress on the drive train as well as adverse acoustic noise [1]. Asymmetrical voltage sag of grid, which can also be regarded as an unbalanced input, often gives a rise to transient overshoot of rotor currents leading to the degraded capability of low voltage ride-through.

The control methods of the Grid Side Converter (GSC) to eliminate input power oscillations at the grid side of rotor under unbalanced input supply have been investigated in past few years. Song and Nam [2] derived dual current control schemes regulating the instantaneous active power under unbalanced input voltage conditions in dq-synchronous frame. Stankovic and Lipo [3] introduced the cases of generalized unbalanced operating conditions. In [4], Suh and Lipo

Paper number: TKPE-2015-20-1-12
Print ISSN: 1229-2214 Online ISSN: 2288-6281
† Corresponding author: ysuh@jbnu.ac.kr, Dept. of Electrical Engineering, Smart Grid Research Center, Chonbuk Nat'l University
Tel: +82-63-270-3381 Fax: +82-63-270-3381
[1] Dept. of Electrical Engineering, Smart Grid Research Center, Chonbuk Nat'l University
Manuscript received Nov. 25, 2014; accepted Dec. 24, 2014
— 본 논문은 2013년 전력전자학술대회 외부장학금 수혜논문임

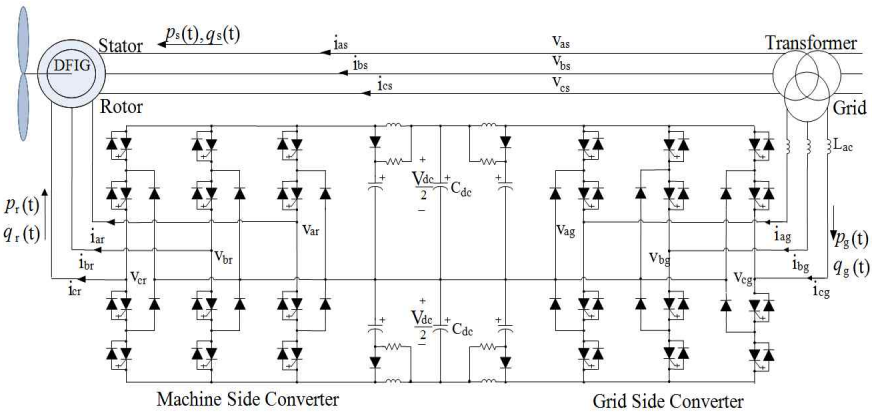

Fig. 1. Overall scheme of DFIG wind turbine system with a back-to-back three-level NPC voltage source converter

have proposed a method to directly control the instantaneous active power at the poles of the rectifier. The proposed control method in [4] can achieve effective elimination of the oscillations under the broad range of unbalanced operating conditions.

Control of the Machine Side Converter (MSC) in DFIG wind power system with a back-to-back converter to reduce torque pulsation by compensating the rotor current under unbalanced grid voltage has been studied in [5] and [6]. The active power ripple flowing into the grid as well as the torque pulsation of DFIG was reduced by controlling MSC under unbalanced grid conditions in [7]. Control method to reduce torque pulsation and rotor current harmonics by compensating negative sequence components utilizing either GSC or MSC was developed in [8]. In [9-13], control methods to eliminate pulsations of torque using MSC and to compensate oscillation of active and reactive power using GSC were presented.

The field of high power drives has been one of the most active parts in research and development of power electronics in last decade including wind turbines [14]. The efficiency and system operational reliability are considered to be key performance factors for large drives because of a growing concern in regard of energy savings and cost [15]. Therefore, the unbalance compensating control algorithms for wind turbine systems of MW range should also take the key performance factors and peculiar features of high power drive systems such as relatively low control bandwidth into consideration. Baier et al. [16] investigated the effect of input unbalance in the case of multicell topology. However, very little works dealing with the practical unbalance compensating control algorithm suitable for high power wind turbines can be found in previous literatures.

In this paper, a grid unbalance compensating control algorithm is proposed for the medium-voltage DFIG wind power system of MW range equipped with a back-to-back three-level neutral-point clamped voltage source converter. The problems generated by unbalanced grid conditions such as overcurrent of rotor, active and reactive power ripples, torque pulsation, and degradation of THD of line currents are evaluated. Using the control laws addressed in [4] and [17], the key performance factors of fault ride-through capability, instantaneous active power pulsation, harmonic distortions, and torque pulsation are investigated. The grid unbalance compensating control algorithm maximizing the key performance factors depending on different grid unbalance conditions for DFIG in medium-voltage wind power system is proposed and validated in this paper.

The paper is structured in three main sections. Section 2 describes the dynamic model of DFIG under unbalanced conditions. The main proposed control algorithm is derived and presented in Section 3. Section 4 discusses the comparison result among several different control algorithms with respect to key performance factors.

2. Dynamic Model of DFIG under Unbalanced Conditions

2.1 DFIG model under unbalanced conditions

Under unbalanced grid voltage, DFIG can be effectively modeled by using both positive and negative sequence components of voltages and currents. The positive and negative sequence components for the voltages of stator and rotor in a synchronous rotating frame are expressed as followings.

$$V_{dqs}^{p} = R_s I_{dqs}^{p} + L_s\left(\frac{d}{dt} I_{dqs}^{p} + jw I_{dqs}^{p}\right) + L_m\left(\frac{d}{dt} I_{dqr}^{p} + jw I_{dqr}^{p}\right) \quad (1)$$

$$\begin{aligned} V_{dqr}^{p} = {} & R_r I_{dqr}^{p} + L_r\left(\frac{d}{dt} I_{dqr}^{p} + j(w - w_r) I_{dqr}^{p}\right) \\ & + L_m\left(\frac{d}{dt} I_{dqs}^{p} + j(w - w_r) I_{dqs}^{p}\right) \end{aligned} \quad (2)$$

$$V_{dqs}^{n} = R_s I_{dqs}^{n} + L_s\left(\frac{d}{dt} I_{dqs}^{n} - jw I_{dqs}^{n}\right) + L_m\left(\frac{d}{dt} I_{dqr}^{n} - jw I_{dqr}^{n}\right) \quad (3)$$

$$\begin{aligned} V_{dqr}^{n} = {} & R_r I_{dqr}^{n} + L_r\left(\frac{d}{dt} I_{dqr}^{n} - j(w + w_r) I_{dqr}^{n}\right) \\ & + L_m\left(\frac{d}{dt} I_{dqs}^{n} - j(w + w_r) I_{dqs}^{n}\right) \end{aligned} \quad (4)$$

In this paper, the direction of stator/rotor current and stator/rotor power are defined using the motor convention, i.e. positive when flowing into the machine winding from the grid. The subscripts 's' and 'r' signify the stator and rotor components. The superscript 's' indicates the stationary reference frame. The superscripts 'p' and 'n' indicate the positive and negative sequence components in CCW-rotating synchronous reference frame and CW-rotating synchronous reference frame, respectively. Under the assumptions of zero resistive voltage drops and steady-state condition, (1) and (3) become

$$V_{dqs}^{p} = j\omega L_s I_{dqs}^{p} + j\omega L_m I_{dqr}^{p} \quad (5)$$

$$V_{dqs}^{n} = -j\omega L_s I_{dqs}^{n} - j\omega L_m I_{dqr}^{n} \quad (6)$$

2.2 Instantaneous output active and reactive power at stator

The instantaneous active power of stator is obtained by taking the real part of the complex power. The instantaneous active power yields the equations of P_{so}, P_{ss2}, and P_{sc2} [4].

$$\begin{aligned} S_s &= \frac{3}{2} V_{dqs}^{s} I_{dqs}^{s*} \\ &= \frac{3}{2}\left(e^{jwt} V_{dqs}^{p} + e^{-jwt} V_{dqs}^{n}\right)\left(e^{jwt} I_{dqs}^{p} + e^{-jwt} I_{dqs}^{n}\right)^{*} \end{aligned} \quad (7)$$

$$p_s(t) = Re\{S_s\} = P_{so} + P_{ss}\sin(2wt) + P_{sc2}\cos(2wt) \quad (8)$$

The instantaneous output reactive power can be developed based on a set of voltages lagging the pole voltages by 90° [4]. A complex quantity, T_s referred as a quadrature complex power is defined and given in (9).

$$\begin{aligned} T_s &= \frac{3}{2} V_{dqs}^{s'} I_{dqs}^{s*} \\ &= \frac{3}{2}\left(-je^{jwt} V_{dqs}^{p} + je^{-jwt} V_{dqs}^{n}\right)\left(e^{jwt} I_{dqs}^{p} + e^{-jwt} I_{dqs}^{n}\right)^{*} \end{aligned} \quad (9)$$

$$q_s(t) = Re\{T_s\} = Q_{so} + Q_{ss}\sin(2wt) + Q_{sc2}\cos(2wt) \quad (10)$$

The active (p_s) and reactive (q_s) power of stator are to be controlled by rotor currents in the DFIG system. Hence, the instantaneous active and reactive power of stator needs to be represented by the positive and negative sequential components of rotor current [12].

2.3 Output torque

The output torque (T_{em}) is obtained from the electromagnetic output power, P_{em}. Electromagnetic output power, P_{em} is directly calculated from the energy conversion term of total output power (P_e).

$$P_e(t) = -\frac{3}{2} Re\left\{V_{dqs}^{s} I_{dqs}^{s*}\right\} - \frac{3}{2} Re\left\{V_{dqr}^{s} I_{dqr}^{s*}\right\} \quad (11)$$

$$\begin{bmatrix} P_{em0} \\ P_{ems2} \\ P_{emc2} \end{bmatrix} = \frac{3L_m w_r}{2L_s w} \begin{bmatrix} V_{ds}^{p} & V_{qs}^{p} & -V_{ds}^{n} & -V_{qs}^{n} \\ -V_{qs}^{n} & V_{ds}^{n} & -V_{qs}^{p} & V_{ds}^{p} \\ -V_{ds}^{n} & -V_{qs}^{n} & V_{ds}^{p} & V_{qs}^{p} \end{bmatrix} \begin{bmatrix} I_{dr}^{p} \\ I_{qr}^{p} \\ I_{dr}^{n} \\ I_{qr}^{n} \end{bmatrix} \quad (12)$$

3. Control Algorithms

3.1 Ripple-free stator power control algorithm (CA1)

The first control algorithm to be investigated in this paper is ripple-free stator power control algorithm. This algorithm is aimed to minimize the ripples of instantaneous active and reactive power at the stator. In Section 2, the average components of stator active and reactive power (P_{so} and Q_{so}) along with the ripple components of instantaneous active power at the stator (P_{ss2} and P_{sc2}) are represented by the sequential components of stator voltage and rotor current. This description is given in (13) and (14).

$$\begin{bmatrix} P_{so} \\ Q_{so} \\ P_{ss2} \\ P_{sc2} \end{bmatrix} = \frac{3}{2} \begin{bmatrix} V_{ds}^{p} & V_{qs}^{p} & V_{ds}^{n} & V_{qs}^{n} \\ V_{qs}^{p} & -V_{ds}^{p} & -V_{qs}^{n} & V_{ds}^{n} \\ V_{qs}^{n} & -V_{ds}^{n} & -V_{qs}^{p} & V_{ds}^{p} \\ V_{ds}^{n} & V_{qs}^{n} & V_{ds}^{p} & V_{qs}^{p} \end{bmatrix} \begin{bmatrix} I_{ds}^{p} \\ I_{qs}^{p} \\ I_{ds}^{n} \\ I_{qs}^{n} \end{bmatrix} \quad (13)$$

$$\begin{bmatrix} I_{ds}^{p} \\ I_{qs}^{p} \\ I_{ds}^{n} \\ I_{qs}^{n} \end{bmatrix} = \frac{1}{wL_s} \begin{bmatrix} V_{qs}^{p} \\ -V_{ds}^{p} \\ -V_{qs}^{n} \\ V_{ds}^{n} \end{bmatrix} - \frac{L_m}{L_s} \begin{bmatrix} I_{dr}^{p} \\ I_{qr}^{p} \\ I_{dr}^{n} \\ I_{qr}^{n} \end{bmatrix} \quad (14)$$

Based on (13) and (14), the positive and negative sequential components of rotor current (I_{dr}^{p}, I_{qr}^{p}, I_{dr}^{n}, and I_{qr}^{n}) can be calculated from four control laws. The

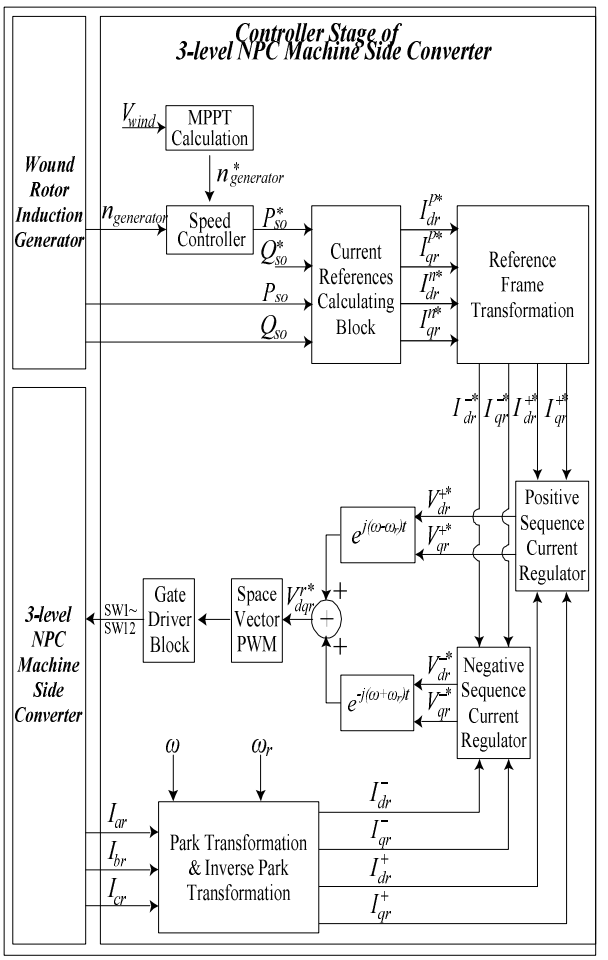

Fig. 2. Control system block diagram of Machine Side Converter

first control law is about the average active power of stator as shown in (15).

$$P_{so} = P_{output} \quad \Rightarrow \quad f_1(I_{dr}^p, I_{qr}^p, I_{dr}^n, I_{qr}^n) = P_{output} \tag{15}$$

The second control law determines the average reactive power of stator described in (16). The average reactive power Q_{so} exchanged between the stator and the grid determines the power factor at the stator side.

$$Q_{so} = 0 \quad \Rightarrow \quad f_2(I_{dr}^p, I_{qr}^p, I_{dr}^n, I_{qr}^n) = 0 \tag{16}$$

The third and fourth control laws are achieved by setting both of P_{ss2} and P_{sc2} to zero thereby nullifying the oscillating components of the instantaneous output active power at the stator.

$$P_{ss2} = 0 \quad \Rightarrow \quad f_3(I_{dr}^p, I_{qr}^p, I_{dr}^n, I_{qr}^n) = 0 \tag{17}$$

$$P_{sc2} = 0 \quad \Rightarrow \quad f_4(I_{dr}^p, I_{qr}^p, I_{dr}^n, I_{qr}^n) = 0 \tag{18}$$

The four rotor current components ($I_{dr}^p, I_{qr}^p, I_{dr}^n$, and I_{qr}^n) are calculated from (15)-(18). The rotor currents in an explicit form are given in the followings.

$$I_{dr}^p = -\frac{2L_s}{3L_m}\frac{V_{ds}^p P_{so}}{(V_{ds}^p)^2+(V_{qs}^p)^2-(V_{ds}^n)^2-(V_{qs}^n)^2} + \frac{V_{qs}^p}{wL_m} \tag{19}$$

$$I_{qr}^p = -\frac{2L_s}{3L_m}\frac{V_{qs}^p P_{so}}{(V_{ds}^p)^2+(V_{qs}^p)^2-(V_{ds}^n)^2-(V_{qs}^n)^2} - \frac{V_{ds}^p}{wL_m} \tag{20}$$

$$I_{dr}^n = \frac{2L_s}{3L_m}\frac{V_{ds}^n P_{so}}{(V_{ds}^p)^2+(V_{qs}^p)^2-(V_{ds}^n)^2-(V_{qs}^n)^2} - \frac{V_{qs}^n}{wL_m} \tag{21}$$

$$I_{qr}^n = \frac{2L_s}{3L_m}\frac{V_{qs}^n P_{so}}{(V_{ds}^p)^2+(V_{qs}^p)^2-(V_{ds}^n)^2-(V_{qs}^n)^2} + \frac{V_{ds}^n}{wL_m} \tag{22}$$

The entire control block diagram for MSC is illustrated in Fig. 2. The current reference calculating block involving (19)-(22) to compute the four rotor current components is also employed in Fig. 2. These four rotor current components are used as reference signals in the dual-frame current regulator for MSC. Therefore, the operation of CA1 using the current control scheme as shown in Fig. 2 ensures that the rotor current has both positive and negative sequential component in a synchronous rotating frame. As a result, the actual rotor current follows these reference values having two frequency terms; positive slip frequency ($\omega-\omega_r$) and negative slip frequency ($\omega+\omega_r$).

3.2 Zero torque ripple control algorithm (CA2)

The second control algorithm to be considered in this paper is zero torque ripple control algorithm (CA2). This control algorithm is designed to minimize the ripple of torque at the shaft of wind turbine. As compared to CA1, this CA2 involves the instantaneous electromagnetic output power instead of instantaneous stator active power to reduce the torque pulsation under grid unbalance operating conditions.

In Section 2, the average component of electromagnetic output power (P_{em0}) along with the ripple components (P_{ems2} and P_{emc2}) are represented by the sequential components of stator voltage and rotor current as shown in (12). The governing equation of reactive power is added into (12) resulting in (23).

$$\begin{bmatrix} P_{em0} \\ Q_{so}^{\wedge} \\ P_{ems2} \\ P_{emc2} \end{bmatrix} = \frac{3L_m w_r}{2L_s w} \begin{bmatrix} V_{ds}^p & V_{qs}^p & -V_{ds}^n & -V_{qs}^n \\ -\frac{w}{w_r}V_{qs}^p & \frac{w}{w_r}V_{ds}^p & \frac{w}{w_r}V_{qs}^n & -\frac{w}{w_r}V_{ds}^n \\ -V_{qs}^n & V_{ds}^n & -V_{qs}^p & V_{ds}^p \\ -V_{ds}^n & -V_{qs}^n & V_{ds}^p & V_{qs}^p \end{bmatrix} \begin{bmatrix} I_{dr}^p \\ I_{qr}^p \\ I_{dr}^n \\ I_{qr}^n \end{bmatrix} \quad (23)$$

In a similar manner as in CA1, the positive and negative sequential components of rotor current (I_{dr}^p, I_{qr}^p, I_{dr}^n, and I_{qr}^n) can be calculated from four control laws based on (23). The first control law is about the electromagnetic output power as shown in (24).

$$P_{em0} = P_{em} \quad \Rightarrow \quad f_1(I_{dr}^p, I_{qr}^p, I_{dr}^n, I_{qr}^n) = P_{em} \quad (24)$$

The second control law is calculated from the average reactive power of stator (Q_{so}) described in (25).

$$Q_{so}^{\wedge} = Q_{so} + \frac{3}{2wL_s}((V_{ds}^p)^2 + (V_{qs}^p)^2 + (V_{ds}^n)^2 + (V_{qs}^n)^2) \quad \Rightarrow \quad f_2(I_{dr}^p, I_{qr}^p, I_{dr}^n, I_{qr}^n) = Q_{so}^{\wedge} \quad (25)$$

The third and fourth control laws are achieved by setting both P_{ems2} of P_{emc2} and to zero thereby nullifying the oscillating components of the electromagnetic torque as shown in followings.

$$P_{ems2} = 0 \quad \Rightarrow \quad f_3(I_{dr}^p, I_{qr}^p, I_{dr}^n, I_{qr}^n) = 0 \quad (26)$$

$$P_{emc2} = 0 \quad \Rightarrow \quad f_4(I_{dr}^p, I_{qr}^p, I_{dr}^n, I_{qr}^n) = 0 \quad (27)$$

The four rotor current components (I_{dr}^p, I_{qr}^p, I_{dr}^n, and I_{qr}^n) are calculated from (24)-(27). The computed rotor currents in an explicit form are given in the followings.

$$I_{dr}^p = \frac{2L_s w}{3L_m w_r} \frac{V_{ds}^p P_{em0}}{(V_{ds}^p)^2 + (V_{qs}^p)^2 - (V_{ds}^n)^2 - (V_{qs}^n)^2} + \frac{V_{qs}^p}{wL_m} \quad (28)$$

$$I_{qr}^p = \frac{2L_s w}{3L_m w_r} \frac{V_{qs}^p P_{em0}}{(V_{ds}^p)^2 + (V_{qs}^p)^2 - (V_{ds}^n)^2 - (V_{qs}^n)^2} - \frac{V_{ds}^p}{wL_m} \quad (29)$$

$$I_{dr}^n = \frac{2L_s w}{3L_m w_r} \frac{V_{ds}^n P_{em0}}{(V_{ds}^p)^2 + (V_{qs}^p)^2 - (V_{ds}^n)^2 - (V_{qs}^n)^2} - \frac{V_{qs}^n}{wL_m} \quad (30)$$

$$I_{qr}^n = \frac{2L_s w}{3L_m w_r} \frac{V_{qs}^n P_{em0}}{(V_{ds}^p)^2 + (V_{qs}^p)^2 - (V_{ds}^n)^2 - (V_{qs}^n)^2} + \frac{V_{ds}^n}{wL_m} \quad (31)$$

The rotor current components are obtained as (28)-(31). These values are used as reference signals in the dual-frame current regulator for MSC employing CA2.

3.3 Single-frame control algorithm (CA3)

The third control algorithm considered in this paper is single-frame control algorithm. This algorithm has only one current regulator for positive sequence components of rotor currents (I_{dr}^p and I_{qr}^p). Therefore, the negative sequential components of rotor current (I_{dr}^n and I_{qr}^n) as well as stator current (I_{ds}^n and I_{qs}^n) cannot be actively regulated due to the limitation of single-frame current regulator. In order to compute the d and q-axis positive sequential component of rotor current (I_{dr}^p and I_{qr}^p), two target conditions; average active power (P_{so}) and average reactive power (Q_{so}) equations should be satisfied. As a result, the upper two rows in the matrix of (13) hold for CA3.

The three-phase switching modulation functions and pole voltages of machine side converter (v_{ar}, v_{br}, and v_{cr}) are set to be balanced having only the component of positive slip frequency ($\omega - \omega_r$) in a single-frame controller as shown in (32). This means that the negative sequence components of rotor current (I_{dr}^n and I_{qr}^n) cannot be regulated thereby resulting in uncontrolled values depending on the depth of unbalance grid voltages.

$$V_{dr}^n = 0, V_{qr}^n = 0 \quad (32)$$

3.4 Proposed unbalance-depth adaptive control algorithm (CA4)

There are many different types of unbalance operating conditions in a grid. In general, the grid unbalance conditions differ in both the depth of unbalance and unbalance duration time. In order to describe the depth of unbalance in a quantitative way, a parameter called Unbalance Factor (UF) is employed throughout this paper. Unbalance Factor (UF) is defined to be the ratio of amplitude of unbalanced phase voltage ($|V_{unbal}|$) to the amplitude of balanced phase voltage ($|V_{bal}|$) as shown in (33).

$$UF = \frac{|V_{unbal}|}{|V_{bal}|} \quad (33)$$

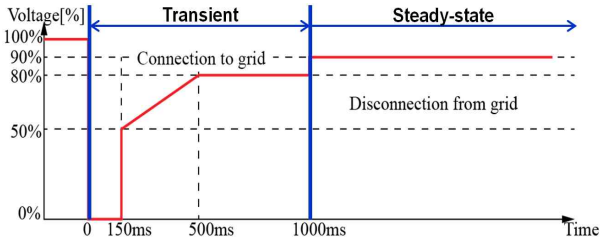

Fig. 3. Typical grid code on low voltage ride-through (KEPCO)

According to various grid codes on low voltage ride-through, the severe unbalance condition having a small value of UF tends to last temporarily, i.e. in the order of tens of milliseconds up to few seconds. In contrary, the relatively shallow grid unbalance condition of large UF may last longer than few seconds or in some cases persist as a steady-state input mode. In Fig. 3, a typical grid code on low voltage ride-through is illustrated. It is required that the wind turbine system be remained to be connected to the grid under the grid fault conditions of the type corresponding to the upper area of red line in Fig. 3. The operation during the unbalance factor of 0.9 and above can be regarded as a steady-state fault condition which can last longer than few seconds irrespective of LVRT, while the unbalance factor of less than 0.9 falls into the transient fault condition lasting for 1 second at maximum as illustrated in Fig. 3.

The four key performance factors of fault ride-through capability, instantaneous active power pulsation, harmonic distortions, and torque pulsation can have different engineering interpretations depending on the depth and duration time of unbalance conditions. For example, fault ride-through capability and instantaneous active power pulsation criteria play a significant role during severe unbalance grid input conditions having a relatively shorter duration time. On the other hand, harmonic distortion and torque pulsation become more critical problem under unbalance grid input conditions having a relatively longer duration time. This is mainly due to the fact that the thermal and mechanical time constants are relatively larger than electrical time constants in a typical wind turbine system. Therefore, it is of high practical importance to select the suitable unbalance control algorithm that satisfies the corresponding key performance factors depending on the depth and duration time of unbalance conditions.

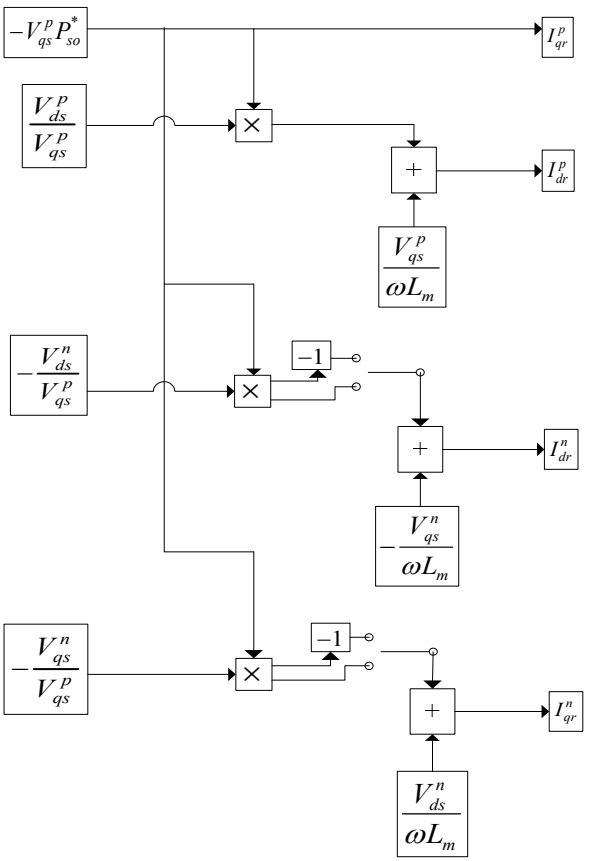

Fig. 4. Detailed current reference calculating block for unbalance-depth adaptive control algorithm

The fourth control algorithm considered in this paper is unbalance-depth adaptive control algorithm. Under the relatively shallow grid unbalance condition, i.e. high unbalance factor(UF≧0.9), zero torque ripple control algorithm (CA2) is adopted in order to minimize torque ripple and current harmonics in a longer time span. As the grid unbalance condition becomes severe, i.e. low unbalance factor (UF<0.9), ripple-free stator power control algorithm (CA1) is chosen due to its superior performance regarding fault ride-through capability and instantaneous active power pulsation. The detailed current reference calculating block for unbalance-depth adaptive control algorithm is described in Fig. 4. The references of current regulator for positive sequence components of rotor currents (I_{dr}^{p} and I_{qr}^{p}) are same under two different control algorithms, i.e. CA1 and CA2. However, the references of negative sequential components of rotor currents (I_{dr}^{n} and I_{qr}^{n}) have different values depending on the unbalance depth as depicted by two switches in Fig. 4.

TABLE I
PARAMETERS OF DFIG WIND TURBINE SYSTEM

Parameter	Symbol	Values
Rated power	P_m	1.5 MW
Rated voltage(line)	V_l	575 V
DC link voltages	V_{dc}	1200 V
Frequency	f	50 Hz
Pole pairs	z_p	2
DC link capacitance	C_{dc}	36 mF
Inertia	J	25 kg.m^2
Gearbox ratio	n	1:75.71
Stator/rotor turns ratio	N	1
Stator resistance	R_s	1.4 mΩ
Rotor resistance	R_r	0.992 mΩ
Stator leakage inductance	L_{ls}	89.98 μH
Rotor leakage inductance	L_{lr}	82.09 μH
Magnetizing inductance	L_m	1.53 mH
Rated wind speed	$V_{w.rated}$	12 m/s
Switching frequency	f_{sw}	10 Khz
Damping resistor	R_{snb}	0.35 Ω
Clamp resistor	C_d	20 μF
di/dt limiting inductor	$L_{di/dt}$	3.5 μH
P-gain of current regulator	K_{pi}	0.0003
I-gain of current regulator	K_{ii}	0.03

4. Comparison of Control Algorithms

In this section, four different control algorithms are compared with respect to four performance factors; FRT capability, active power pulsation, harmonic distortions, and torque pulsation. The simulation is made based on the operating condition specified in Table 1. The parameters have been adopted from a GE 1.5MW turbine [18 and 19].

There are many different types of unbalance operating conditions. Among these, the single-phase under-voltage unbalance condition, i.e. type-B in [20], is the most popular type of unbalance encountered during a single-line fault condition in grid network. In this paper, four different control algorithms are compared under this single-phase under-voltage unbalance condition of type-B. In order to effectively evaluate four unbalance control algorithms, unbalance factor of 0.5 and 0.9 are selected in the simulation verification.

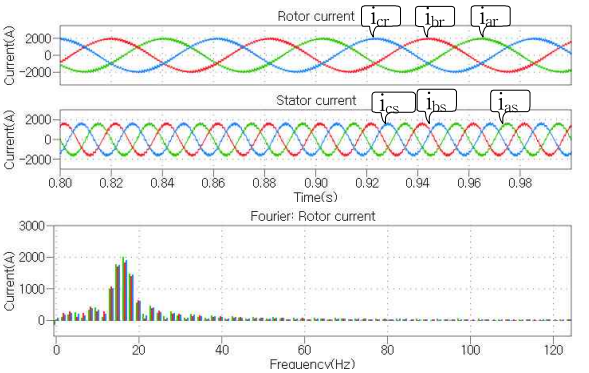

Fig. 5. Stator and rotor current (Balanced)

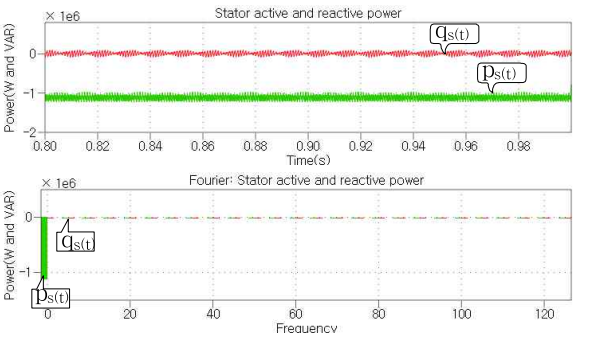

Fig. 6. Active and reactive instantaneous power of stator (Balanced)

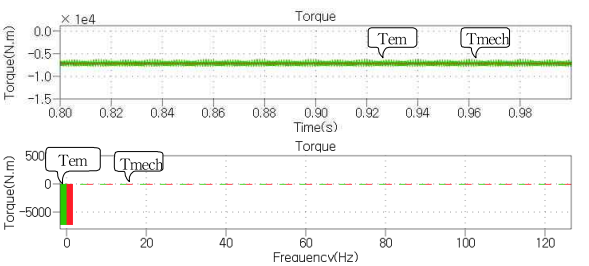

Fig. 7. Electromagnetic torque from DFIG and mechanical torque from blade (Balanced)

Under the balanced grid network condition, i.e. UF=1, all four control algorithms show similar performances since the all negative sequential components become nullified. The key operational waveforms under the balanced condition are described in Fig. 5-7. In Fig. 5, the stator currents and rotorr currents are illustrated. The frequency spectrum of rotor current is also shown in Fig. 5. Active and reactive instantaneous power of stator are obtained and shown in Fig. 6 along with its frequency spectrum. Figure 7 shows the mechanical torque from blade and electromagnetic torque from DFIG. The frequency spectrum of two torque values is also described in Fig. 7.

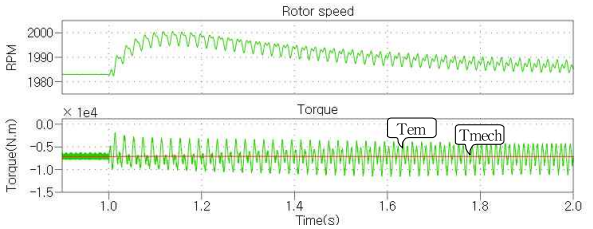

Fig. 8. Rotor speed, electromagnetic torque from DFIG, and mechanical torque from blade (UF=1 to 0.5 at t=1.0 s,CA1)

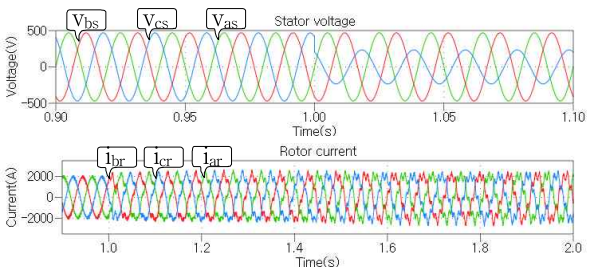

Fig. 9. Stator voltage and rotor current (UF=1 to 0.5 at t=1.0s, CA1)

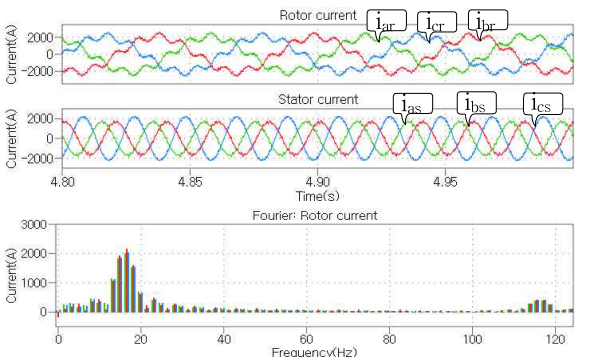

Fig. 10. Stator and rotor current (UF=0.5, CA1)

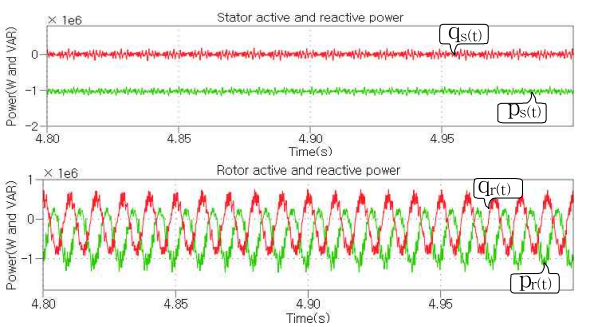

Fig. 11. Active and reactive instantaneous power of stator and rotor (UF=0.5, CA1)

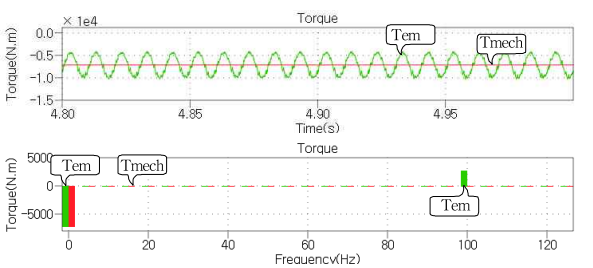

Fig. 12. Electromagnetic torque from DFIG and mechanical torque from blade (UF=0.5, CA1)

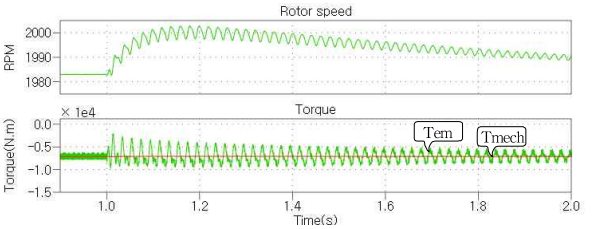

Fig. 13. Rotor speed, electromagnetic torque from DFIG, and mechanical torque from blade (UF=1 to 0.5 at t=1.0s , CA2)

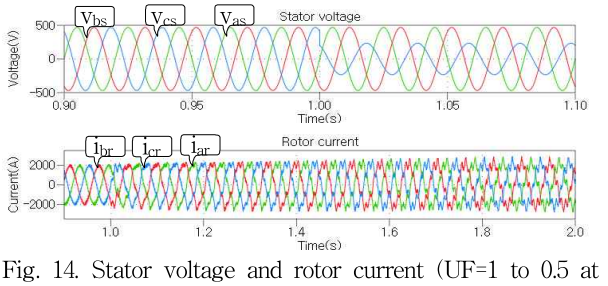

Fig. 14. Stator voltage and rotor current (UF=1 to 0.5 at t=1.0s, CA2)

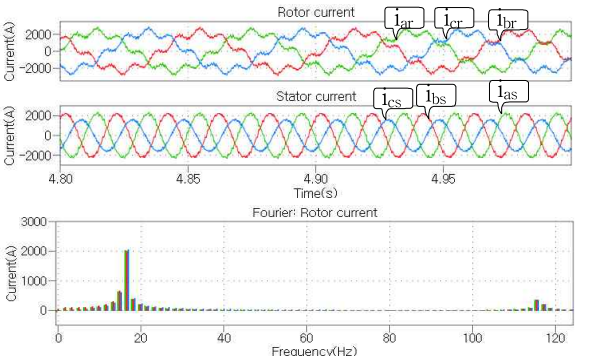

Fig. 15. Stator and rotor current (UF=0.5, CA2)

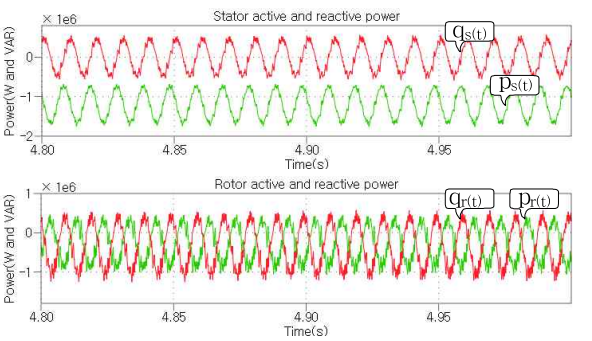

Fig. 16. Active and reactive instantaneous power of stator and rotor (UF=0.5, CA2)

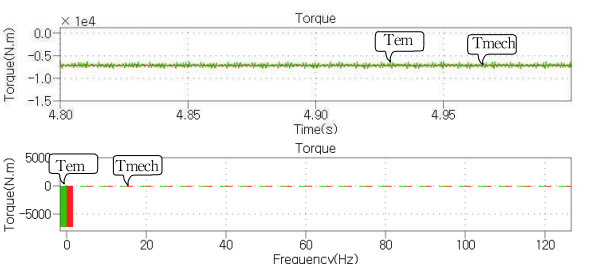

Fig. 17. Electromagnetic torque from DFIG and mechanical torque from blade (UF=0.5, CA2)

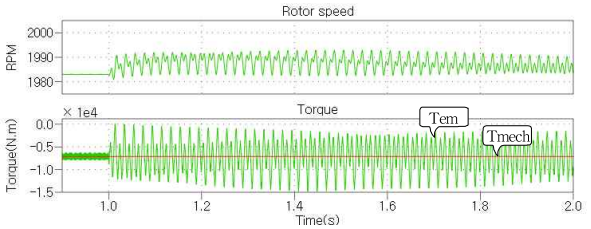

Fig. 18. Rotor speed, electromagnetic torque from DFIG, and mechanical torque from blade (UF=1 to 0.5 at t=1.0s, CA3)

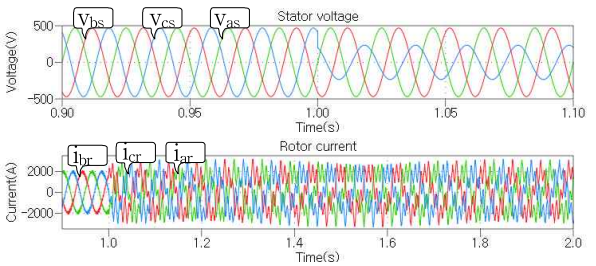

Fig. 19. Stator voltage and rotor current (UF=1 to 0.5 at t=1.0s, CA3)

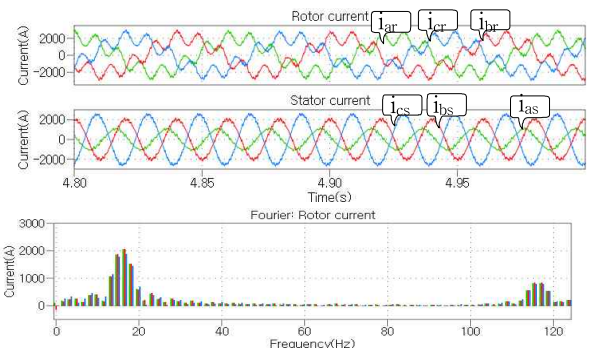

Fig. 20. Stator and rotor current (UF=0.5, CA3)

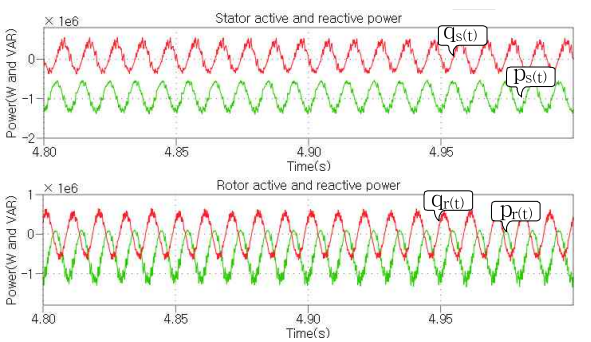

Fig. 21. Active and reactive instantaneous power of stator and rotor (UF=0.5, CA3)

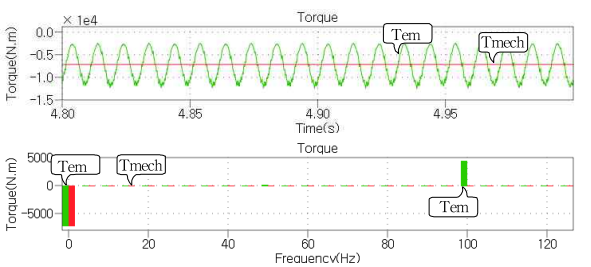

Fig. 22. Electromagnetic torque from DFIG and mechanical torque from blade DFIG (UF=0.5, CA3)

TABLE II
CURRENT REFERENCES FOR EACH CONTROL ALGORITHM (UF=0.5)

Component	Balanced	Unbalanced	
		CA1	CA2
v_{as} [V]	$470\sin(wt)$	$470\sin(wt)$	$470\sin(wt)$
v_{bs} [V]	$470\sin(wt+240^\circ)$	$470\sin(wt+240^\circ)$	$470\sin(wt+240^\circ)$
v_{cs} [V]	$470\sin(wt+120^\circ)$	$235\sin(wt+120^\circ)$	$235\sin(wt+120^\circ)$
i_{as} [A]	$-1582\sin(wt)$	$-1677\sin(wt-11^\circ)$	$-2202\sin(wt+9^\circ)$
i_{bs} [A]	$-1582\sin(wt+240^\circ)$	$-1677\sin(wt+251^\circ)$	$-2202\sin(wt+231^\circ)$
i_{cs} [A]	$-1582\sin(wt+120^\circ)$	$-2196\sin(wt+120^\circ)$	$-1524\sin(wt+120^\circ)$
i_{ar} [A]	$1940\sin((w-w_r)t-31^\circ)$	$2103\sin((w-w_r)t-22^\circ)$ $+420\sin((w+w_r)t+262^\circ)$	$2247\sin((w-w_r)t-21^\circ)$ $+449\sin((w+w_r)t+39^\circ)$
i_{br} [A]	$1940\sin((w-w_r)t+209^\circ)$	$2103\sin((w-w_r)t+217^\circ)$ $+420\sin((w+w_r)t+22^\circ)$	$2247\sin((w-w_r)t+219^\circ)$ $+449\sin((w+w_r)t+159^\circ)$
i_{cr} [A]	$1940\sin((w-w_r)t+89^\circ)$	$2103\sin((w-w_r)t+97^\circ)$ $+420\sin((w+w_r)t+142^\circ)$	$2247\sin((w-w_r)t+99^\circ)$ $+449\sin((w+w_r)t-81^\circ)$
I_{ds}^{p} [A]	0	0	0
I_{qs}^{p} [A]	1582	1830	1977
I_{ds}^{n} [A]	0	317	-343
I_{qs}^{n} [A]	0	183	-198
I_{dr}^{p} [A]	-978	-815	-815
I_{qr}^{p} [A]	-1655	-1938	-2094
I_{dr}^{n} [A]	0	-417	281
I_{qr}^{n} [A]	0	-53	351

Under the condition of 50% single-phase unbalance, i.e. UF=0.5, control algorithms of CA1, CA2, and CA3 are evaluated through simulation. At the simulation time of 1 sec, the unbalance factor has been decreased from 1 to 0.5 in a step-wise manner. The simulation waveforms corresponding to CA1 are given in Fig. 8-12. The corresponding simulation waveforms for CA2 and CA3 are also shown in Fig. 13-17 and Fig. 18-22, respectively. As in the case of simulation waveforms for balanced condition, waveforms of same circuit variables are presented for each control algorithm.

TABLE Ⅲ
PERFORMANCE FACTORS OF EACH CONTROL ALGORITHM (UF=0.5)

Factors	CA1	CA2	CA3
Stator active power ripple at 100 Hz	12 kW	462 kW	364 kW
Torque ripple at 100 Hz	2732 Nm	8 Nm	4471 Nm
Transient peak rotor current	2758 A	2922 A	3322 A
THD of stator current	7 %	6 %	11 %

The reference values of stator and rotor current utilized in each control algorithm as well as grid input voltages under the condition of UF=0.5 are summarized in Table 2. Under the balanced grid network, the frequency of rotor current equals to the rotor slip frequency, $\omega^{-}\omega_r$. However, under the unbalanced grid conditions, rotor currents have a negative sequence component of $\omega^{+}\omega_r$ in addition to a positive sequence component of $\omega^{-}\omega_r$. This negative sequence component of $\omega^{+}\omega_r$ can be found in Fig. 10, 15, and 20.

It is noted from Fig. 11, 16, and 21 that the unbalanced ac grid condition causes the major harmonic component of instantaneous active and reactive power at the twice input line frequency, i.e. 100Hz. As in Section 3, CA1 produces the least amount of harmonic component of instantaneous active and reactive power among all three control algorithms. It is interesting to note that the ripple sizes of instantaneous active and reactive power are the same. This observation is in line with the argument that the instantaneous active and reactive powers have the same ripple size in time domain [4].

Ripples of electromagnetic torque for three different control algorithms are compared in Fig. 12, 17, and 22. Same as the instantaneous active and reactive power, the dominant harmonic component of torque is produced at the twice input line frequency under unbalanced operating conditions. Among three different control algorithms, CA2 generates the least amount of harmonic component of electromagnetic torque as explained in Section 3.

The performance factors of each control algorithm obtained from simulation are summarized and presented in Table 3 for the condition of UF=0.5. These factors include ripple size of stator active and reactive instantaneous power at 100Hz, torque ripple at 100Hz, peak values of rotor currents, and THD of stator currents.

TABLE Ⅳ
CURRENT REFERENCES FOR EACH CONTROL ALGORITHM (UF=0.9)

Component	Balanced	Unbalanced	
		CA1	CA2
v_{as} [V]	$470\sin(wt)$	$470\sin(wt)$	$470\sin(wt)$
v_{bs} [V]	$470\sin(wt+240^\circ)$	$470\sin(wt+240^\circ)$	$470\sin(wt+240^\circ)$
v_{cs} [V]	$470\sin(wt+120^\circ)$	$422\sin(wt+120^\circ)$	$422\sin(wt+120^\circ)$
i_{as} [A]	$-1582\sin(wt)$	$-1607\sin(wt-2^\circ)$	$-1667\sin(wt-3^\circ)$
i_{bs} [A]	$-1582\sin(wt+240^\circ)$	$-1607\sin(wt+242^\circ)$	$-1667\sin(wt+237^\circ)$
i_{cs} [A]	$-1582\sin(wt+120^\circ)$	$-1691\sin(wt+120^\circ)$	$-1582\sin(wt+120^\circ)$
i_{ar} [A]	$1940\sin((w-w_r)t-31^\circ)$	$1972\sin((w-w_r)t-29^\circ)+68\sin((w+w_r)t+269^\circ)$	$1976\sin((w-w_r)t-28^\circ)+68\sin((w+w_r)t+31^\circ)$
i_{br} [A]	$1940\sin((w-w_r)t+209^\circ)$	$1972\sin((w-w_r)t+211^\circ)+68\sin((w+w_r)t+29^\circ)$	$1976\sin((w-w_r)t+211^\circ)+68\sin((w+w_r)t+152^\circ)$
i_{cr} [A]	$1940\sin((w-w_r)t+89^\circ)$	$1972\sin((w-w_r)t+91^\circ)+68\sin((w+w_r)t+149^\circ)$	$1976\sin((w-w_r)t+91^\circ)+68\sin((w+w_r)t-89^\circ)$
I_{ds}^{p} [A]	0	0	0
I_{qs}^{p} [A]	1582	1634	1638
I_{ds}^{n} [A]	0	48	-49
I_{qs}^{n} [A]	0	28	-28
I_{dr}^{p} [A]	-978	-946	-946
I_{qr}^{p} [A]	-1655	-1731	-1735
I_{dr}^{n} [A]	0	-68	36
I_{qr}^{n} [A]	0	-1	58

TABLE Ⅴ
PERFORMANCE FACTORS OF EACH CONTROL ALGORITHM (UF=0.9)

Factors	CA1	CA2	CA3
Stator active power ripple at 100 Hz	0 kW	77 kW	90 kW
Torque ripple at 100 Hz	487 Nm	8 Nm	980 Nm
Transient peak rotor current	2238 A	2194 A	2405 A
THD of stator current	6 %	7 %	7 %

Fault and low voltage ride-through capability are becoming a more and more important performance factor in wind power system because of the grid-friendly connection requirement on wind farms. In general, DFIG wind power system suffers a lot from a relatively weak FRT capability due to an absence of full-rated power converter between the machine and the grid. A typical grid code requires that during the voltage sag condition, wind turbines should continue its power generation and voltage support without tripping the system. The most common failure or shut-down mechanism of DFIG wind power system under the voltage sag condition is over current triggered trip. This particular unbalance condition, i.e. voltage sag, induces unbalanced rotor current resulting in transient over current and higher overshoot current. From the simulation result, CA1 generates the smallest value of peak rotor current among three different control algorithms as shown in Table 3. In other words, by employing CA1, the DFIG system has better ability to generate rated power and maintain voltage support without tripping MSC in a complete PCS under severe unbalance conditions, i.e. voltage sag.

In this paper, the simulation result under the shallow unbalance depth of UF=0.9 is also given. The calculated current reference values along with grid input voltages are summarized in Table 4. The four key performance factors are also obtained for each control algorithm and summarized in Table 5. Due to space limitation, the waveforms for each control algorithm under the condition of UF=0.9 are not provided in this paper. In fact, the characteristics of each control algorithm presented in the waveforms of Fig. 8-22 for the case of UF=0.5 also appear under the shallow unbalance depth of UF=0.9. As noted in Table 3 and 5, CA1 provides the smallest stator active power ripple, while CA2 offers the smallest torque ripple among different control algorithms. As for the transient peak value of rotor current and THD of stator current, the case of shallow unbalance depth (UF=0.9) exhibits different characteristics from those of the deeper unbalanced case (UF=0.5). CA2 has the smallest transient peak value of rotor current, while CA1 shows the least THD of stator current. However, the difference between the transient peak values of rotor current for CA1 and CA2 is relatively small, i.e. the difference of 44 A as compared to 164 A of the deeper unbalanced case (UF=0.5). Also, three different control algorithms show similar THD values within 1%. Therefore, it is found that the performance factors of stator active power ripple and torque ripple play a major determining role under the shallow unbalance depth.

Unbalance-depth adaptive control algorithm (CA4) proposed in this paper selects either the CA1 or CA2 depending on the grid unbalance depth. Under the shallow unbalance depth ($UF \geqq 0.9$), it selects CA2, while it switches to CA1 under the severe grid unbalance condition ($UF < 0.9$). Therefore it achieves the optimized performance factors of fault ride-through capability, instantaneous active power pulsation, harmonic distortions, and torque pulsation depending on the grid unbalance depth. The performance of unbalance-depth adaptive control algorithm (CA4) has been verified through simulation and the comparison of its performance against CA1 and CA2 are provided in Fig. 23-26. In these figures, the unbalance depth is altered from UF=0.9 to UF=0.5 at t=1.0s and from UF=0.5 to UF=0.9 at t=1.15s in a step-wise manner representing a dynamic fault condition from the grid. Therefore, unbalance-depth adaptive control algorithm (CA4) maintains the mode of CA2 until t=1.0s and switches to CA1 at t=1.0s. At the moment of t=1.15s, CA4 now switches back to CA2 from CA1. All these mode changes are done automatically depending on the measured unbalance factor (UF) as explained in Fig. 4.

The electromagnetic torque from DFIG along with mechanical torque from blade for the case of CA1 is shown in Fig. 23. The same waveforms for the case of CA4 are given in Fig. 24. It is clearly noted from Fig. 23 and 24 that the ripple of electromagnetic torque during steady-state condition of UF=0.9 before t=1.0s has the lower value in the case of CA4. The torque ripple usually gives a meaningful impact on the drive train of wind turbine in a longer time frame, i.e. in the range of mechanical time constant. In contrary to the torque ripple, the transient peak value of rotor current becomes a critical factor of fault ride-through capability during a much shorter dynamic fault condition such as in the time range from t=1.0 to t=1.15s. The transient rotor currents for the case of CA2 and CA4 are illustrated in Fig. 25 and 26, respectively. The proposed algorithm of CA4 generates the less peak value (3137 A) of rotor current as compared to the case of CA2 (2719 A). This reduction of peak rotor current due to CA4 may

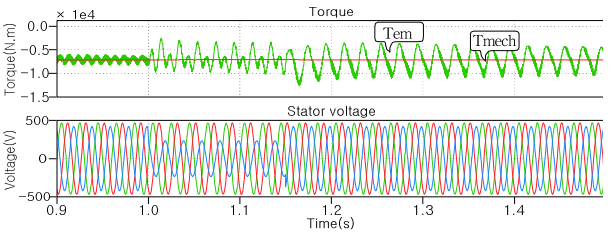

Fig. 23. Transient electromagnetic torque from DFIG and mechanical torque from blade (CA1, UF 0.9 to 0.5 at t=1.0s and 0.5 to 0.9 at t=1.15s)

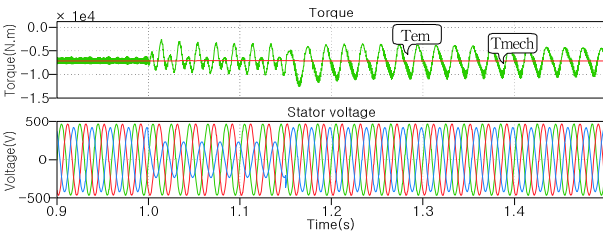

Fig. 24. Transient electromagnetic torque from DFIG and mechanical torque from blade (Unbalance-depth adaptive control algorithm(CA4), UF 0.9 to 0.5 at t=1.0s and 0.5 to 0.9 at t=1.15s)

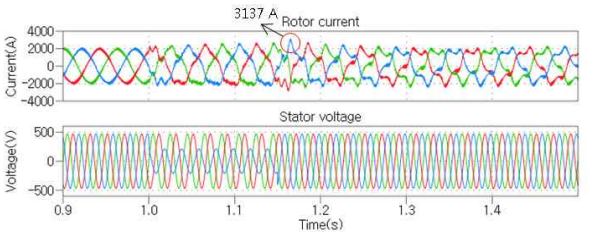

Fig. 25. Transient rotor current and stator voltage (CA2, UF 0.9 to 0.5 at t=1.0s and 0.5 to 0.9 at t=1.15s)

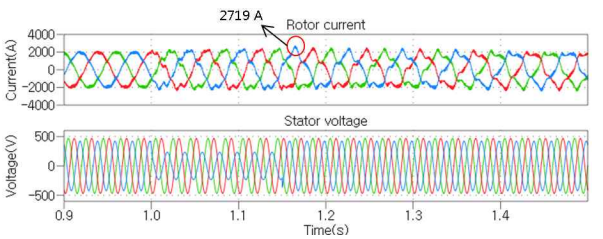

Fig. 26. Transient rotor current and stator voltage (Unbalance-depth adaptive control algorithm(CA4), UF 0.9 to 0.5 at t=1.0s and 0.5 to 0.9 at t=1.15s)

decrease the chance of over current trip and malfunctioning of dc-link chopper circuit so that the more reliable and efficient fault ride-through operational scheme is made possible.

5. Conclusions

This paper investigates unbalance compensating control algorithms for a doubly fed induction wind generator employing a back-to-back three-level NPC voltage source converter. Four different control algorithms have been devised based on instantaneous active, reactive power of stator and torque. These algorithms are compared with respect to FRT capability, stator active power ripple, harmonic distortions and torque pulsation. Control algorithm 2 having torque ripple set to zero shows the most optimized and cost-effective performance in terms of torque pulsation. Control algorithm 1 that nullifies the oscillating components of the instantaneous stator active power surpasses the other two algorithms regarding stator active power pulsation. The unbalance adaptive control algorithm (CA4) which combines control algorithm 1 and 2 depending on the depth of grid unbalance is proposed in this paper. By employing the unbalance adaptive control algorithm, four performance factors such as FRT capability, stator active power pulsation, harmonic distortions, and torque pulsation can be improved selectively under the generalized unbalanced grid conditions leading to high performance DFIG wind turbine system. The proposed control algorithms are verified through transient response in the simulation.

This work was supported by the National Research Foundation of Korea (NRF) grant funded by the Korea government (MSIP) (No. 2010-0028509).

This work was supported by the National Research Foundation of Korea (NRF) grant funded by the Korea government (MSIP) (No. 2014R1A2A1A11053678).

References

[1] E. Muljadi, T. Batan, D. Yildirim, and C. P. Butterfield, "Understanding the unbalanced-voltage problem in wind turbine generation," *in Conference proceedings of IAS 1999*, pp. 1359-1365, 1999.

[2] H. Song and K. Nam, "Dual current control scheme for pwm converter under unbalanced input voltage conditions," *IEEE Transactions on Industrial Electronics*, Vol. 46, No. 5, pp. 953-959, Oct. 1999.

[3] A. Stankovic and T. A. Lipo, "A generalized control method for input-output harmonic elimination for the PWM boost type rectifier under simultaneous unbalanced input voltages and input impedances," *in Conference proceedings of PESC*, pp. 1309-1314, 2001.

[4] Y. S. Suh and T. A. Lipo, "Control scheme in hybrid synchronous stationary frame for PWM AC/DC converter under generalized unbalanced operating conditions," *IEEE Transactions on Industry Applications*, Vol. 42, No. 3, pp. 825-835, May/June 2006.

[5] T. Brekken and N. Mohan, "A novel doubly-fed induction wind generator control scheme for reactive power control and torque pulsation compensation under unbalanced grid voltage conditions," *in Conference proceedings of PESC 2003*, Vol. 2, pp. 760 - 764, Jane 2003.

[6] T. Brekken and N. Mohan, "Control of a doubly fed induction wind generator under unbalanced grid voltage condition," *IEEE Transactions on energy conversion*, Vol. 22, No. 1, pp. 129-135, Mar. 2007.

[7] A. G. Abo-Khalil, D. C. Lee, and J. I. Jang, "Control of back-to-back PWM converters for DFIG wind turbine systems under unbalanced grid voltage," *IEEE Industrial Electronics International Symposium*, pp. 2637-2642, June 2007.

[8] L. Fan, H. Yin, and R. Kavasseri, "Negative sequence compensation techniques of DFIG-based wind energy systems under unbalanced grid conditions," *IEEE Power Electronics and Machines in Wind Applications*, pp 1-6, June 2009.

[9] L. Xu, "Coordinated control of DFIG's rotor and grid side converters during network unbalance," *IEEE Transactions on Power Electronics*, Vol. 23, No. 3, pp. 1041-1049, May 2008.

[10] Y. Wang, L. Xu, and B. W. Williams, "Control of DFIG-based wind farms for network unbalance compensation," *IEEE Power Electronics Specialists Conference*, pp 113-119, June 2008.

[11] W. Qiao and R. G. Harley, "Improved control of DFIG wind turbines for operation with unbalanced network voltages," *IEEE Industry Applications Society Annual Meeting*, pp. 1-7, Oct. 2008.

[12] J. Hu and Y. He, "Reinforced control and operation of DFIG-based wind-power-generation system under unbalanced grid voltage conditions," *IEEE Transactions on Energy Conversion*, Vol. 24, No. 4, pp 905-915, Dec. 2009.

[13] L. Xu and Y. Wang, "Dynamic modeling and control of DFIG-based wind turbines under unbalanced network conditions," *IEEE Transactions on Power Systems*, Vol. 22, No. 1, pp. 314-323, Feb. 2007.

[14] J. Rodriguez, S. Bernet, B. Wu, J. O. Pontt, and S. Kouro, "Multilevel voltage-source-converter topologies for industrial medium-voltage drives," *IEEE Transactions on Industrial Electronics*, Vol. 54, No. 6, pp. 2930 - 2945, Dec. 2007.

[15] Y. S. Suh, J. Steinke, and P. Steimer, "Efficiency comparison of voltage source and current source drive system for medium voltage applications," *IEEE Transactions on Industrial Electronics*, Vol. 54, No. 5, pp. 2521 - 2531, Oct. 2007.

[16] C. R. Baier, J. I. Guzman, J. R. Espinoza, M. A. Perez, and J. R. Rodriguez, "Performance evaluation of a multicell topology implemented with single-phase nonregenerative cells under unbalanced supply voltages," *IEEE Transactions on Industrial Electronics*, Vol. 54, No. 6, pp. 2969 - 2978, Dec. 2007.

[17] Y. S. Suh, Y. R. Go, and D. H. Rho, "A comparative study on control algorithm for active front-end rectifier of large motor drives under unbalance Input," *IEEE Transactions on Industrial Electronics*, Vol. 47, No. 3, pp. 1419 - 1431, May/June 2011.

[18] J. Schönberger, "Modeling a DFIG wind turbine system using Plecs," *Application note of Plexim GmbH*, pp 2969-2978, Dec. 2008.

[19] N. Miller, W. Price, and J. Sanchez-Gasca, "Dynamic modeling of GE 1.5 and 3.6 MW wind turbine generators," *Technical Report, GE Power Systems Energy Consulting*, 2003.

[20] M. Bollen, "Characterisation of voltage sags experienced by three-phase adjustable-speed drives," *IEEE Transactions on Power Delivery*, Vol. 12, No. 4, pp. 1666-1671, Oct. 1997.

[21] O. S. Ebrahim, P. K. Jain, and G. Nishith, "New control scheme for the wind-driven doubly fed induction generator under normal and abnormal grid voltage conditions," *Journal of Power Electronics*, Vol. 8, No. 1, pp. 10-22, Jan. 2008.

[22] V. T. Phan, H. H. Lee, and T. W. Chun, "An effective rotor current controller for unbalanced stand-alone DFIG systems in the rotor reference frame," *Journal of Power Electronics*, Vol. 10, No. 6, pp. 724-732, Nov. 2010.

[23] Y. Park, D. Han, and Y. Suh, "Minimization of active power and torque ripple for a doubly fed induction generator in medium voltage wind power systems under unbalanced grid conditions," *Journal of Power Electronics*, Vol. 13, No. 6, pp. 1032-1041, Nov. 2013.

Daesu Han was born in Korea in 1987. He received his B.S. in Electrical Engineering from Chonbuk National University, Jeonju, Korea, in 2013, where he is currently working toward his M.S. in Electrical Engineering. His current research interests include the power conversion systems of high power for renewable energy sources and medium electric drive systems.

Yongsug Suh was born in Seoul, Korea. He received his B.S. and M.S. in Electrical Engineering from Yonsei University, Seoul, Korea, in 1991 and 1993, respectively, and his Ph.D. in Electrical Engineering from the University of Wisconsin, Madison, WI, USA, in 2004. From 1993 to 1998, he was an Application Engineer in the Power Semiconductor Division of Samsung Electronics Co. From 2004 to 2008, he was a Senior Engineer in the Power Electronics and Medium Voltage Drives Division of ABB, Turgi, Switzerland. Since 2008, he has been with the Department of Electrical Engineering, Chonbuk National University, Jeonju, Korea, where he is currently an Associate Professor. His current research interests include the power conversion systems of high power for renewable energy sources and medium voltage electric drive systems.